Effects of non-Lambertian surfaces on integrating sphere measurements

L. M. Hanssen

The effects of non-Lambertian scattering of the interior wall of an integrating sphere are examined through a sphere simulation model. The model employs Monte Carlo techniques. A sphere used for measurement of directional–hemispherical reflectance is modeled. The simulation allows sphere wall scattering to vary from perfectly Lambertian to perfectly specular in steps. The results demonstrate that significant measurement error can result as the scattering deviates from the Lambertian ideal. The error is found to be a strong function of the wall reflectance value as well: it is minimized for reflectances approaching 1.0 and increases as the reflectance value decreases to the minimum value examined of 0.5. The magnitudes of the errors associated with non-Lambertian scattering are also shown to be relatively independent of the specific field of view of the detector used in the measurement.

1. Introduction

The integrating sphere is a versatile optical device with many uses that include averaging of optical radiation for detection, attenuation of high power levels for detection, creation of a uniform Lambertian source, and measurement of the optical properties of diffusely scattering materials. Successful use of an integrating sphere as an optical device generally requires that its interior surface scatters light in a perfectly Lambertian fashion over the wavelength region of interest. If the interior surface scatters radiation in a non-Lambertian fashion, then the basic assumptions for the standard integrating sphere analysis are violated and the resulting equations may lose their validity.

For use in the infrared (IR) spectral region (2–20 μm), integrating spheres typically employ a diffuse gold coating, which is a surface scatterer. Gindele and Köhl examined the scattering characteristics of such a sphere in 1987 and discovered a strong tendency toward specular scattering at longer wavelengths.[1] They measured a specularity factor that corresponds to the fraction of light scattered in the specular direction for near-normal incidence, increasing from the ideal value corresponding to diffuse scattering at 2 μm to ~50% at 20 μm. Under such circumstances, the sphere behaves in an unconventional fashion. IR integrating spheres are nevertheless used, and measurement results are based on equations assuming ideal coating behavior.[2]

Hence, important questions that need to be answered are: is the assumption of the applicability of the ideal integrating sphere equations a valid one, and what size potential error (and hence uncertainty in the measurement) could one anticipate? What are the circumstances, if any, under which the uncertainties are acceptably small, and do the ideal equations produce reasonable results?

Although extensive analysis and a large number of papers describe many details and effects of integrating sphere designs on measurement performance, analytical solutions almost always assume ideal Lambertian scattering.[3–7] The situation of nonideal sphere coating behavior is a difficult one to tackle analytically in any general way.[8] Thus we take a different approach. The scattering and absorption of light in the sphere are handled in a Monte Carlo statistical fashion. The sphere behavior is simulated through ray tracing of a large number of individual rays. To simulate a sample measurement, the program simply keeps track of the number of rays absorbed at the detector port. Preliminary results of the sphere wall specularity study were presented at the 1992 Council for Optical and Radiation Measurement annual meeting.[9]

In the following sections the effects of sphere wall specularity are examined. In Section 2 details of the simulation model, how the Monte Carlo technique is applied, and the important assumptions are presented. The model used to describe sphere wall

The author is with the Optical Technology Division, National Institute of Standards and Technology, Gaithersburg, Maryland 20899.

Received 24 February 1995; revised manuscript received 18 December 1995.

scattering within the simulation program is described in Section 3. Results from examinations of the integrating sphere throughput and reflectance measurement are presented in Subsection 4.A. Simulation results of the irradiance distribution within the integrating sphere are discussed in Subsection 4.B. The effects of wall reflectance and the detector field of view on sphere measurements are examined in Subsections 4.C and 4.D, respectively. Finally a discussion of the implications of the results on integrating sphere designs and the accuracy of measurements in the infrared is presented in Section 5.

2. Integrating Sphere Simulation Model

To analyze the performance of an integrating sphere through a simulation program, we set up an integrating sphere with appropriate ports and trace individual rays until they are absorbed. Through the accumulation of data from a large number of rays, sufficiently low uncertainty can be achieved to obtain meaningful results.

The integrating sphere geometry used in the simulation was chosen as representative of a typical sphere designed with a high degree of symmetry for optimum accuracy.[10] The geometry is shown in Fig. 1. Sample and reference ports are positioned symmetrically with respect to an entrance port as well as to the detector port. There are no baffles and the sample and reference are assumed to be curved to match the shape of the sphere wall. Since all the surfaces that interact with the rays lie on a single spherical surface, only two surface coordinates and two direction angles are required to trace rays in the sphere. Consequently the analyses and results described in the following sections apply to any diameter sphere, with port diameters scaled accordingly. Specifically, the diameter of all the ports (in radians) is $\pi/18$; this corresponds to a 2.5-cm port diameter for a 15-cm sphere diameter. For Fig. 8, the detector diameter is $\pi/9$.

In the simulation, individual rays are sent into the sphere by way of the entrance port and followed until they are absorbed or lost from the sphere. One can simulate a collimated beam by randomly selecting the ray's input position within a beam radius ($\pi/72$)

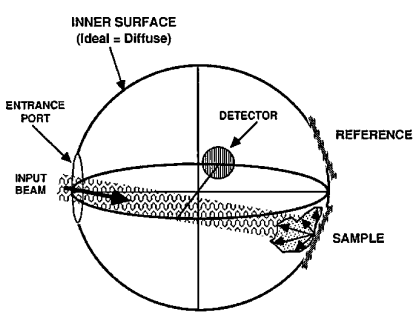

Fig. 1. Typical integrating sphere geometry used in the simulation analyses. The centers of the entrance, sample, and reference ports lie in a great circle, whereas the normal to the detector port passes through the center of that great circle.

of the entrance port center. The ray is traced across the sphere to its intersection with a port or the sphere wall. At this point, absorption may take place (if a randomly selected number between 0 and 1 is greater than the wall reflectivity). If the ray is absorbed, it is cataloged and a new ray trace is begun from the entrance port. If the ray is not absorbed, a scattering direction is randomly selected from the probability distribution matched to the sphere wall scattering properties. The ray is again traced across the sphere to the next intersection point. The procedure is repeated until absorption takes place. Then new rays are traced in the same manner until the requisite total number of rays is attained.

To simulate a directional hemispherical reflectance measurement, we first direct the input beam onto the sample, and the rays absorbed at the detector are recorded. Then the reference is irradiated and the rays absorbed at the detector are again recorded. The ratio of these two measurements is the measured reflectance. Use of these two terms in Section 4 refers specifically to simulation results. The 2σ uncertainty for each is approximately given by $2/\sqrt{N}$, where N is the number of rays absorbed at the detector.

The simulation program assumes, as stated above, that all the surfaces are curved to match the sphere wall. Polarization effects are not considered and all the surfaces are assumed to be spatially uniform.

The simulation program is written in FORTRAN 77. Versions of the program were run on both Cray Research Y-MP and Macintosh IIfx computers.[11] Most of the results described in this paper were generated using the latter computer. Comparisons of results from both computers showed agreement. The number of rays used in the simulation runs ranged from 50,000 to 1,000,000.

3. Sphere Wall Scattering Model

Incorporation of nondiffuse sphere wall scattering is implemented through a simple model in which ideal diffuse scattering is linearly mixed with ideal specular scattering. The specific mixture is denoted as the specularity factor s, defined as the ratio of the energy in the specular component divided by the total energy. Such a simple model can be expected to emulate qualitatively the effects of a range of nondiffuse scattering profiles. In analogous studies of the effects of diffuse and specular coatings on blackbody cavities, a similar model was used.[12,13]

A schematic of the scattering model is shown in Fig. 2. Illustrations of four cases with specularity factors of 0 (perfectly diffuse), 0.5, 0.75, and 1.0 (perfectly specular) are shown.

4. Simulation Results

Now we examine the effects of the specularity on the behavior of an integrating sphere used for reflectance measurements. Specific values of parameters are used in the simulation runs; these are selected to represent values associated with typical

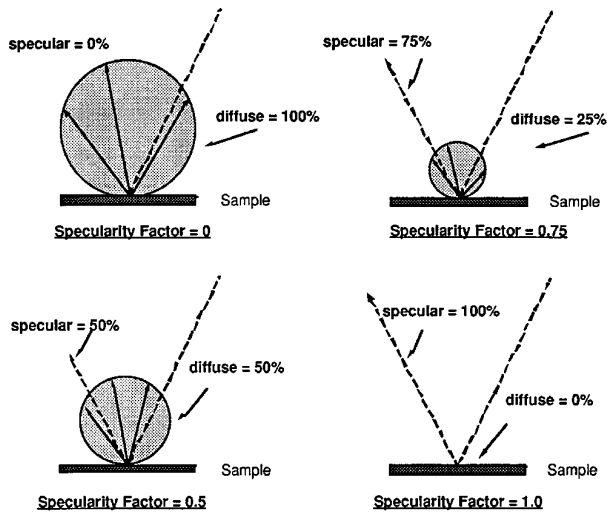

Fig. 2. Diagrams showing scattering distributions from the sphere wall coating used in the simulation program. The distributions are a combination of perfectly specular and perfectly diffuse components. The specularity factor, defined as the ratio of the flux contained in the specularly reflected beam to that of the input beam, is fixed for a particular analysis. Each sketch represents a particular combination of specular and diffuse scattering for the coating.

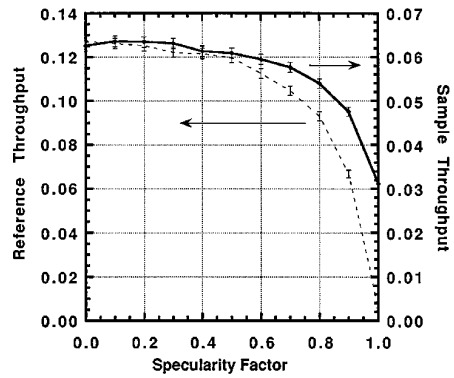

Fig. 3. Plot of integrating sphere throughput (relative fraction of input flux falling on the detector port) versus specularity factor for sample and reference measurements showing steeper falloff of the throughput with specularity for the reference than for the sample.

integrating spheres. Even though the simulation results will vary quantitatively depending on the specific parameter values that are selected, the important qualitative aspects of the results should not vary significantly. The directional–hemispherical (diffuse) reflectance of the sphere sections are selected, unless otherwise noted, as follows: 0.95 for the sphere wall (typical for infrared diffuse gold), 0.5 for the sample, 0.0 for the detector, and 0.95 for the reference (1.0 in Figs. 3–7). The sphere wall and reference angular scattering character are assumed to be identical and are characterized by the specularity factor as described in Fig. 2.

The sample scattering is chosen to be perfectly Lambertian (diffuse) in order to extract possible measurement error information. If the sample and reference have identical scattering character, there will be no measurement error (at least for a properly designed sphere). However, a difference in scattering character between the sample and reference will lead to measurement error for spheres with nonideal characteristics.[10]

A. Sphere Throughput and Reflectance Measurement

To examine a simulated reflectance measurement under the conditions described above, simulation runs were performed for the input beam incident on the sample and reference. The resulting fractions of incident light on the sample and reference, which are absorbed by the detector, are referred to as the sample throughput and reference throughput, respectively. The results of a series of sample and reference throughput measurements are shown in Fig. 3 as a function of sphere wall specularity. For an ideal sphere, the throughputs should be in the ratio of 2:1 (reference reflectance:sample reflectance) for a specularity factor of 0. The sample throughput axis is shown with a scale corresponding to half of the reference throughput, because the sample reflectance is half of the reference reflectance. Both curves fall off as the specularity factor s increases, but the reference throughput falls off faster. This is because the light reflecting off a specular reference and sphere wall will remain in the plane of incidence and stay away from the detector. Thus, if one finds an integrating sphere with a similar geometry, which has an anomalously low throughput, a partially specular coating may be the cause.

Even for a perfectly specular case ($s = 1$), the reference throughput is nonzero because some of the rays eventually hit the diffuse sample and scatter out of the plane of incidence. Because of the statistical variations associated with the finite number of rays traced, some irregular structure in the curves appears in Fig. 3 as well as in later figures. One can reduce this structure by increasing the total number of rays traced, but the computation time would also have to be increased.

The sample reflectance can be obtained through a ratio of the sample and reference throughput measurements. This ratio is normally equal to the ratio of the sample and reference reflectances according to standard sphere theory. Because the reference reflectance is selected to be 1.0, the ratio should equal the sample reflectance (0.5). The results of ratioing the curves from Fig. 3 are shown in Fig. 4. The measured reflectance of the sample is plotted as a function of the specularity factor. For $s = 0.0$, the measured reflectance is close to 0.5. But, as the specularity factor is increased, the measured reflectance increases gradually at first and then more dramatically. Clearly, this indicates that a sphere with a specularity factor >0.5 cannot be used with confidence.

B. Irradiance Distribution within a Sphere

Given a specific specularity factor, is there a different sphere geometry for which the measurement

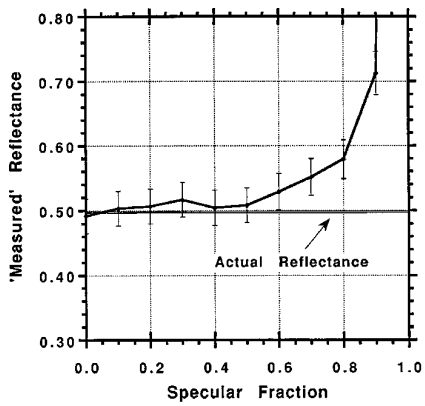

Fig. 4. Simulated measured reflectance value versus specularity factor. The sample reflectance value used in the simulation is 0.5. The error bars represent 3σ for each data point.

errors are reduced? To answer this question we need to examine the irradiance distribution over the sphere wall interior. This can be done in the simulation by simply counting reflections within small sphere area elements and dividing by the area of each element.

The coordinate systems used for the irradiance distribution plots are shown in Figs. 5 and 6. The sphere is shown with its ports and coordinate system of two angles θ and ϕ, which define any point (θ, ϕ) on its surface. θ ranges from 0 to π, and ϕ from 0 to 2π.

For the purpose of displaying the entire sphere surface in a single plot, rectangular plots are used in Figs. 7–9. The locations of the ports are shown in Fig. 6. Note that $\phi = 2\pi$ corresponds to $\phi = 0$, so that the sample and reference ports are split between the right and left sides of the plot, yet are connected at $\phi = 0$ and 2π.

The irradiance as well as the absorbed radiation is monitored in the simulation over a 90×90 grid (of $2° \times 4°$ elements). The grid elements vary in area from a maximum size at $\theta = 90°$ to a minimum size at $\theta = 0°$ and $\theta = 180°$. For the ideal perfectly Lambertian (0 specularity factor) case, we expect the irradiance to be uniform over the sphere wall except for the input beam spot, and we expect the absorbed

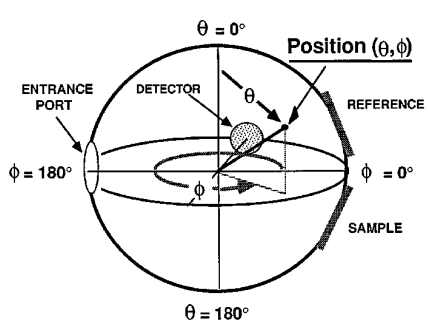

Fig. 5. Definition of the coordinate system used for the description of the simulation results: θ and ϕ are standard spherical coordinates that define the position of any point on the sphere surface.

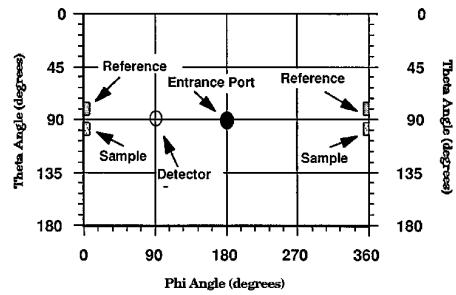

Fig. 6. Two-dimensional map of the sphere surface with coordinate system (theta [θ], phi [ϕ]), as defined in Fig. 5, and location of the ports indicated.

light density to be uniform over the sphere wall except for the port areas.

The absorbed light density and the irradiance are plotted in Figs. 7(a) and 7(b), respectively, for the $s = 0$ specularity case. The input beam spot has been subtracted from Fig. 7(b) revealing the irradiance uniformity over the sphere wall. To the right of plots (a) and (b) scales in arbitrary units show the correspondence between the color level and absorbed density and irradiance, respectively. These plots show noise near the top and bottom. This is the result of the small area and the correspondingly small number of rays incident and absorbed on these grid elements. When the data shown in Figs. 7(a) and 7(b) are smoothed by averaging over three grid elements in both the θ and ϕ directions, the results are as shown in Figs. 7(c) and 7(d), respectively. The smoothed data show the uniformity of the irradiance [Fig. 7(d)] over the entire sphere wall, and the absorbed density [Fig. 7(c)] over the sphere wall except for the ports. In this case only, the detector port is twice the diameter of the other ports.

Now let us examine the effects of sphere wall specularity as described in Fig. 2. The irradiance distribution is shown in Fig. 8. A pair of plots is shown for each selection of sphere wall specularity factor s. The upper set of plots represents the results for input beam incidence on the sample, whereas the lower set of plots represents input beam incidence on the reference. The color scale is in arbitrary units. However, all the plots in Figs. 8 and 9 are on the same relative scale: values are consistent for all the plots. To facilitate comparison, the range of the color scale for the sample incidence plots relative to the reference incidence plots was compressed by a factor of 2 to compensate for the lower reflectance of the sample. In addition, all the plots have been normalized by the number of rays used in each simulation.

For $s = 0$, the only difference between the sample and reference cases is the greater irradiance values associated with the input beam spots located at $(\theta, \phi) = (100°, 0°)$ and $(80°, 0°)$, respectively. For reference incidence, as s increases, greater irradiance appears where the series of specular reflections off the reference and sphere wall occur. The increases in irradiance take place in and near the plane of

Fig. 7. (a) Absorbed light and (b) irradiance distribution for the ideal zero specularity case. Plots (c) and (d) are the same data as (a) and (b), respectively, smoothed by averaging over three grid elements in both the θ and ϕ directions. Note the statistical noise that results in deviations from a perfectly uniform irradiance distribution.

incidence ($\phi = 0$, π, and 2π) whereas the decreases in irradiance take place away from the plane as s increases from 0 through 1. For sample incidence, as s increases, greater irradiance appears directly opposite the sample on the sphere wall.

Note that the most uniform regions of the sphere surface for all the values of s are centered at $(\theta, \phi) = (\pi/2, \pi/2)$ and $(\pi/2, 3\pi/2)$; this is where the detector and its field of view, respectively, are centered. The detector signal is proportional to the intensity at the $(\pi/2, \pi/2)$ location. As s increases the irradiance at this location decreases for both sample and reference incidence, but decreases more for reference incidence. Hence, the measured reflectance, which is the ratio of the sample and reference irradiances, increases with s, just as is shown in Fig. 4.

For some sphere wall scattering profiles that differ from the model assumed in this paper, it is easy to predict the results qualitatively by examining the results shown in Fig. 8. For example, for scattering that exhibits a lobe around the specular direction, one would expect the specular reflection spots in the irradiance plots as in Fig. 8 to be larger and weaker, with somewhat greater irradiance values at the detector location. Nevertheless, one would still expect the general results of Subsections 4.A–4.C: that the measured sample reflectance values would be greater than the true reflectance.

C. Effects of Wall Reflectance Value

An important variable that affects the performance of all integrating spheres is sphere wall reflectance. In general, the lower the sphere wall reflectance, the greater the potential measurement error that is due to any deviation from ideal behavior. The results previously discussed were derived for a sphere wall reflectance value of 0.95. How does the irradiance distribution change for differing wall reflectance values? A comparison of irradiance distributions for sample and reference incidence is shown in Fig. 9 for wall reflectance values of 0.5 and 0.975. The specularity factor for both sets of plots is 0.5. In both sample and reference incidence plots, for greater wall reflectance (0.975) the irradiance distribution is more uniform than for the comparable plots in Fig. 8, whereas for the 0.5 case, the uniformity of the irradiance distribution is significantly worse than the Fig. 8 plots.

As in Fig. 4, measured reflectance values are plotted in Fig. 10. Using the data from a series of irradiance distribution simulation runs, reflectance measurements were simulated for sphere wall reflectance values ranging from 0.5 to 0.975. The sample reflectance values were obtained by ratioing the smoothed irradiance values at the detector position for sample incidence to the values for reference incidence and multiplying the result by the reference

Fig. 8. Irradiance distribution for (a) sample incidence and (b) reference incidence for specularity factors ranging from 0.0 to 0.9375. Note the imaging of the input spot in (a) of the diffuse sample, on the opposite side of the sphere. Note changes in the distribution, increasing irradiance in the plane of incidence and decreasing irradiance out of this plane. Also note in (b), the increasing intensity corresponding to the specular component reflections off the sphere wall.

reflectance (also equal to the wall reflectance). Each data point in Fig. 10 represents a measured sample reflectance for a specific specularity factor and wall reflectance value. For high values of sphere wall reflectance, the error in the measured reflectance is small (<0.02) even for specularity factor values as high as 0.5; only for nearly complete specularity does the error become large. For lower values of sphere wall reflectance, on the other hand, the error in the measured reflectance becomes signifi-

Fig. 9. Irradiance distribution comparison for two wall reflectance values with the same specularity factor of 0.5. The plots to the left [(a) and (b)] are for wall reflectance of 0.5, and the plots to the right [(c) and (d)] are for a wall reflectance of 0.975. Upper [(a) and (c)] and lower [(b) and (d)] plots are for sample and reference incidence, respectively.

cant for progressively lower specularity factor values. There is some crossover of the curves, where the statistical variations are of the order of the differences between the curves.

D. Interaction with Detector Field of View

The detector field of view often comes into play in the error analysis of integrating spheres. Almost every detector will have some effective limitation to its field of view, either directly through apertures and baffling or indirectly through a falloff in sensitivity as a function of incidence angle. This is especially true in the infrared spectral region for which detectors that operate at cryogenic temperatures are required.[14,15] Since the irradiance distribution over the sphere wall is not uniform and since a restricted detector field of view samples an asymmetrically irradiated portion of the sphere, an examination of the directional distribution of light irradiating the detector is warranted. Perhaps an enlightened choice of detector field of view might reduce the measurement errors associated with a hemispherical field of view (assumed in Subsections 4.A. and 4.C.).

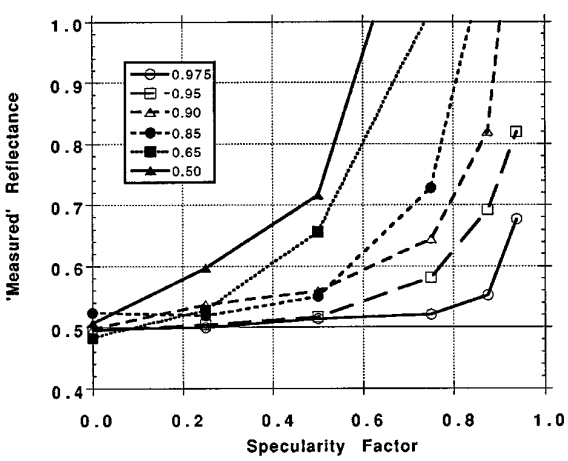

Fig. 10. Measured reflectance versus specularity factor. Each curve corresponds to a different wall reflectance value ranging from 0.5 to 1.0, with the specific values shown in the legend inset.

A series of simulation runs was performed, for which the absorbed rays at the detector were grouped and counted according to their incident angles on the detector. The results for sphere wall reflectance of 0.95 and specularity factor of 0.75 are shown in Figs. 11 and 12. Both incident (Θ) and azimuthal (Φ) angles with respect to the detector normal were examined.

The results shown in Fig. 11 indicate that, even for a high degree of specularity, the incident angular distribution of light on the detector is close to the ideal case [combination of Lambertian illumination $\sin(2\Theta)$ and a hot spot] obtained for 0 specularity

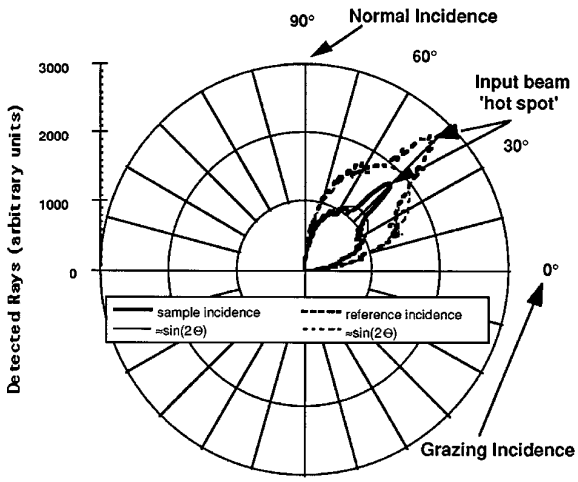

Fig. 11. Number of rays absorbed at the detector versus incident angle (Θ) on the detector. The sphere wall reflectance is 0.95 and the specularity factor is 0.75. Curves are shown for both sample (smaller values) and reference incidence (larger values). Overlaid with the simulation results solid curves represent the dashed curves expected from ideal sphere behavior (except for the hot spot lobes). The large structure(s) for $\Theta = \pi/2$ are theoretically expected and arise from the more intense input beam spot on the sphere wall.

factor. Even for the $s = 0$ case, a hot spot corresponding to the initial reflection off the sphere wall can be seen by the detector. In many sphere designs this is removed from the detector field of view by a baffle or other field-of-view limitation. The deviation from $\sin(2\Theta)$ in Fig. 11 reflects a combination of increased flux level from the input beam spot on the sample and reference and a decreased flux level from the empty entrance port and low reflectance sample. This can be seen more clearly in Fig. 13. Although the shapes of the curves' two main features (Lambertian component and hot spot) are the same as would be obtained for an ideal sphere wall, the relative flux levels of these two components are appreciably different for the high degree of specularity case shown in Fig. 11. The greater the specularity factor, the greater the flux contribution from the hot spot and the smaller the contribution from the Lambertian component. In addition, as discussed below, the hot spot component in Fig. 11 is distributed throughout the entire azimuthal angular range, so that it no longer can be considered a spot and be blocked by a baffle.

An examination of the azimuthal angular distribution of incident light on the detector is shown in Fig. 12. Note that the entrance port is located at $\Phi = 270°$, the sample port at 100°, and the reference port at 80°. For sample incidence the distribution can be divided into roughly three components: one from the hot spot on the sample where the input beam is incident, a second from the image of the hot spot on the opposite side of the sphere at $\Phi = 270°$, and a third uniform component corresponding to Lambertian illumination. From Fig. 12 it can be seen that, for sample incidence, the peak at $\Theta = 45°$ seen in Fig. 11 is made up of flux from both the hot spot and its image. For reference incidence, the curve in Fig. 12 evidences the specularity of the reference and sphere wall through a series of washed out peaks decreasing in intensity and corresponding to the series of specular reflections within the sphere. In Fig. 12, the peaks are located at $\Phi = (80°, 250°, 60°, 230°, 40°,$

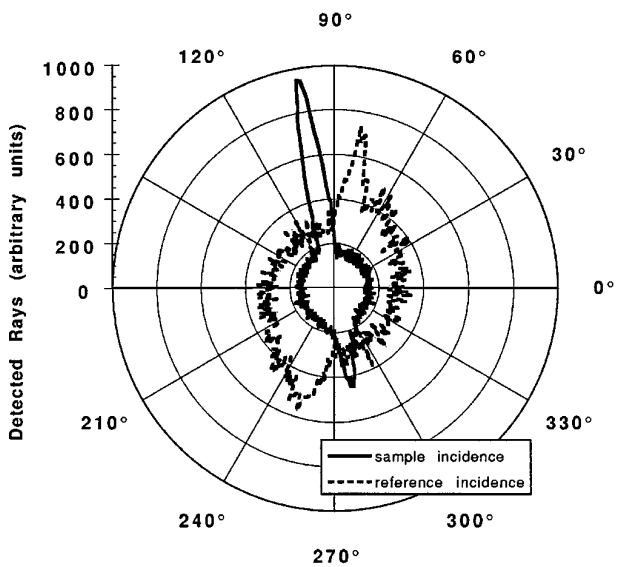

Fig. 12. Number of rays absorbed at the detector versus azimuthal angle (Φ) incident on the detector. The sphere wall reflectance is 0.95 and the specularity factor is 0.75. Curves are shown for sample and reference incidence. The peak structures for sample incidence arise from the input beam hot spot at $\Phi = 100°$ and its associated image directly opposite at $\Phi = 280°$. For reference incidence, the peak structures correspond to successively weaker specular reflections, back and forth across the sphere.

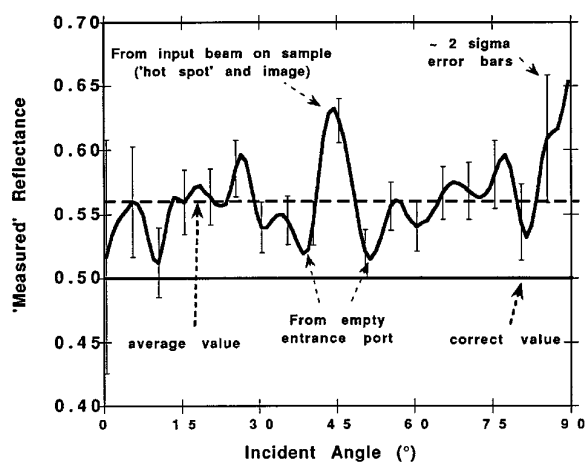

Fig. 13. Measured reflectance value as a function of incident angle of light onto the detector. The reflectance value does not vary from the average, except in the region of the hot ring. Hence the detector FOV should not affect the error that is due to the specularity: if the FOV includes the hot ring region, the system may be more susceptible to other errors and imperfections. Hence, in general it would be advisable to shield the hot ring from the detector.

210°, 20°, 190°, etc.). Hence, the term hot ring might be more appropriate than hot spot. A residual Lambertian illumination can be discerned from this reference incidence curve as with the sample incidence curve. A minimum corresponding to the entrance port can be seen at 270°.

To gauge the effect of restricting the detector field of view on the reflectance measurement, we divided the two curves shown in Fig. 11 to obtain the reflectance versus incident angle plot shown in Fig. 13. The curve represents the reflectance that would be measured by the detector for light incident only at an angle Θ on the detector. Each incident angle defines a thin walled cone of light. Additional lines in Fig. 13 indicate the correct sample reflectance (solid) and the average measured reflectance (dashed). The width (5°) of the peak at 45° corresponds to the input beam spot diameter at the sample and reference, whereas the dips on either side of the peak correspond to the entrance and sample port diameters (10°). Because the number of detected rays falls to zero close to $\Theta = 0°$ and 90°, the uncertainty increases correspondingly ($\sim 1/\sqrt{N}$) at these two extremes.

Except for the region around the hot spot, the error bars overlap the average measured value for every incident angle. Note that the average value of 0.565 differs slightly from the ~0.58 value in Fig. 10. These values were obtained in separate runs and reflect the expected statistical variations. For any specific detector field of view (FOV), the resulting reflectance would be the normalized integral of the measured reflectance over incident angles (Θ) from 0° to the FOV half-angle, weighted by $\cos(\Theta)$. From the results shown in Fig. 13, this value would be roughly constant and equal to the hemispherical FOV case.

Therefore, apparently the detector FOV does not play a significant role in its interaction with the sphere wall specularity source of error. That is, neither does a reduced or restricted FOV increase the size of the error substantially, nor can it be adjusted to decrease somehow the error size significantly. This is not to say that a restricted detector FOV cannot contribute to large measurement errors through interaction with other sources of error, as has been shown (see Refs. 2 and 9). Limiting the detector FOV to remove the hot ring component around $(\Theta, \Phi) = (45°, 0° \text{ to } 360°)$ would be advisable to reduce the variability of irradiance with sample scattering distribution from this region. Note that simple baffles between the sample and reference and the detector are insufficient in the case of a nonzero specular component.

5. Summary and Conclusions

A numerical calculation approach employing Monte Carlo methods has been used to analyze the effects of non-Lambertian scattering from the interior wall of an integrating sphere. In particular, an analysis is made of the wall's scattering properties effects on diffuse reflectance measurements. Both the specularity and the magnitude of the wall reflectance are found to affect the accuracy of such measurements significantly. The effects of a limited detector field of view have been examined. The errors associated with a nonzero wall specularity factor are seen to be fairly independent of the detector field of view, except for the region corresponding to the hot ring, where the incident light in the sphere is concentrated by the focusing properties of the partially specular spherical mirror.

The importance of the diffuse character of sphere wall scattering has been affirmed and it has been shown that the errors associated with deviations from the ideal need to be taken into account, especially in the case of high accuracy measurements.

High sphere wall reflectance has been shown to have the benefit (in addition to greater throughput and hence an improved signal-to-noise ratio) of reducing the errors associated with nonideal wall scattering. The wavelength dependence of both a sphere's wall reflectance and its scattering character will result in a wavelength dependence of the errors that are due to non-Lambertian scattering.

As is the case with other sources of error, the lower reflectance values of integrating sphere coatings in the IR compared with the visible significantly worsen the potential measurement error that is due to non-Lambertian coating behavior. The size of the error as a function of wavelength depends on the net result of two counteracting effects: the increased specular character of sphere wall scattering with increased wavelength, and the increased reflectance with wavelength.

References and Notes

1. K. Gindele and M. Köhl, "Strengths and weaknesses of IR-active integrating spheres," Sol. Energy Mater. **16,** 167–172 (1987).
2. R. R. Willey, "Results of a round robin measurement of spectral emittance in the mid-infrared," in *Passive Infrared Systems and Technology,* H. M. Lamberton, ed., Proc. SPIE **807,** 140–147 (1987).
3. A. H. Taylor, "The measurement of diffuse reflection factors and a new absolute reflectometer," J. Opt. Soc. Am. **4,** 9–23 (1920).
4. A. H. Taylor, "Errors in reflectometry," J. Opt. Soc. Am. **25,** 51–56 (1935).
5. J. A. Jacquez and H. F. Kuppenheim, "Theory of the integrating sphere," J. Opt. Soc. Am. **45,** 460–470 (1955).
6. F. J. J. Clarke and J. A. Compton, "Correction methods for integrating sphere measurement of hemispherical reflectance," Color Res. Appl. **11,** 253–262 (Winter 1986).
7. H. L. Tardy, "flat-sample and limited-field effects in integrating sphere measurements," J. Opt. Soc. Am. A **5,** 241–245 (1988).
8. H. L. Tardy, "Matrix method for integrating-sphere calculations," J. Opt. Soc. Am. A **8,** 1411–1418 (1991).
9. L. M. Hanssen, "Effects of non-Lambertian surfaces on integrating sphere measurements," presented at the Council for Optical and Radiation Measurement 1992 Annual Meeting,

New Carrolton, Md., 19–20 May 1992, Program and Book of Abstracts, p. 8.
10. K. A. Snail and L. M. Hanssen, "Integrating sphere designs with isotropic throughput," Appl. Opt. **28,** 1793–1799 (1989).
11. The mention of manufacturers and model names is intended solely for the purpose of technical information useful to the reader and in no way should be construed as an endorsement of the named manufacturer or product.
12. A. Ono, "Calculation of the directional emissivities of cavities by the Monte Carlo Method," J. Opt. Soc. Am. **70,** 547–554 (1980).
13. V. I. Sapritsky and A. V. Prokhorov, "Calculation of the effective emissivities of specular-diffuse cavities by the Monte Carlo Method," Metrologia **29,** 9–14 (1992).
14. L. M. Hanssen and K. A. Snail, "Infrared diffuse reflectometer for spectral, angular, and temperature resolved measurements," in *Passive Infrared Systems and Technology,* H. M. Lamberton, ed., Proc. SPIE **807,** 148–159 (1987).
15. L. M. Hanssen, "Effects of restricting the detector field of view when using integrating spheres," Appl. Opt. **28,** 2097–2103 (1989).

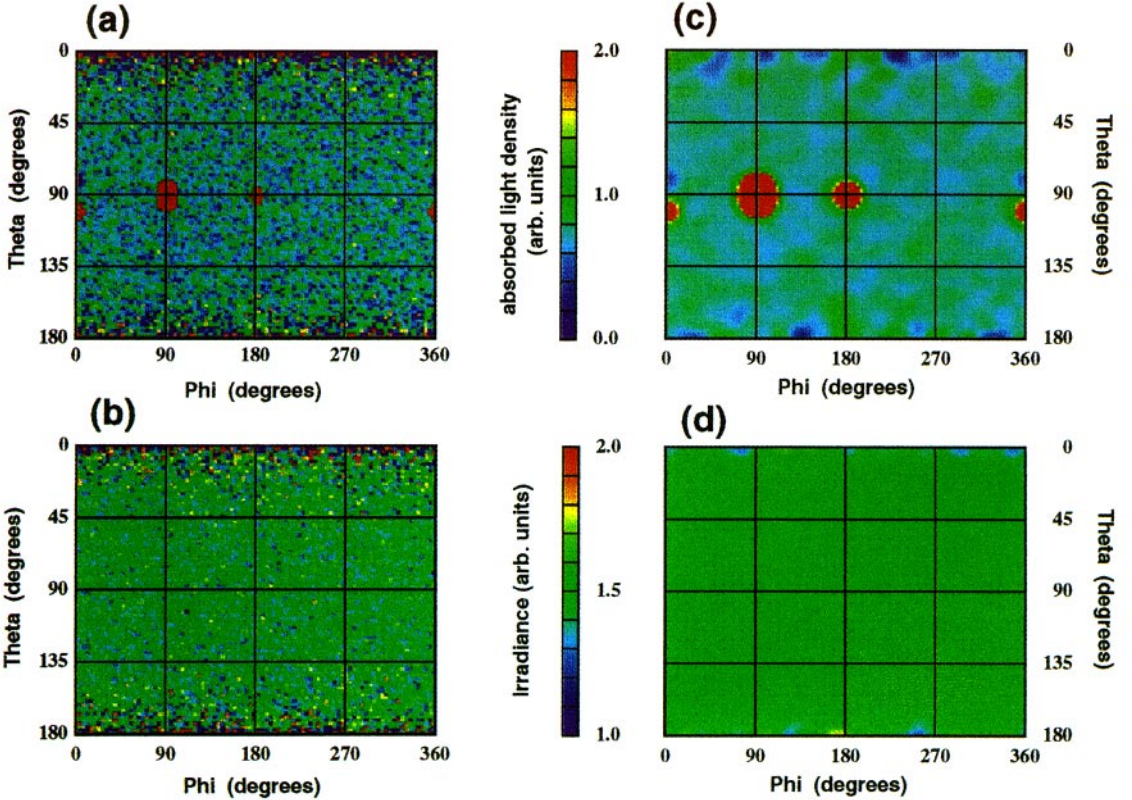
(a)
(b)
(c)
(d)
Theta (degrees)
Phi (degrees)
0
45
90
135
180
0
90
180
270
360
absorbed light density (arb. units)
2.0
1.0
0.0
Irradiance (arb. units)
2.0
1.5
1.0

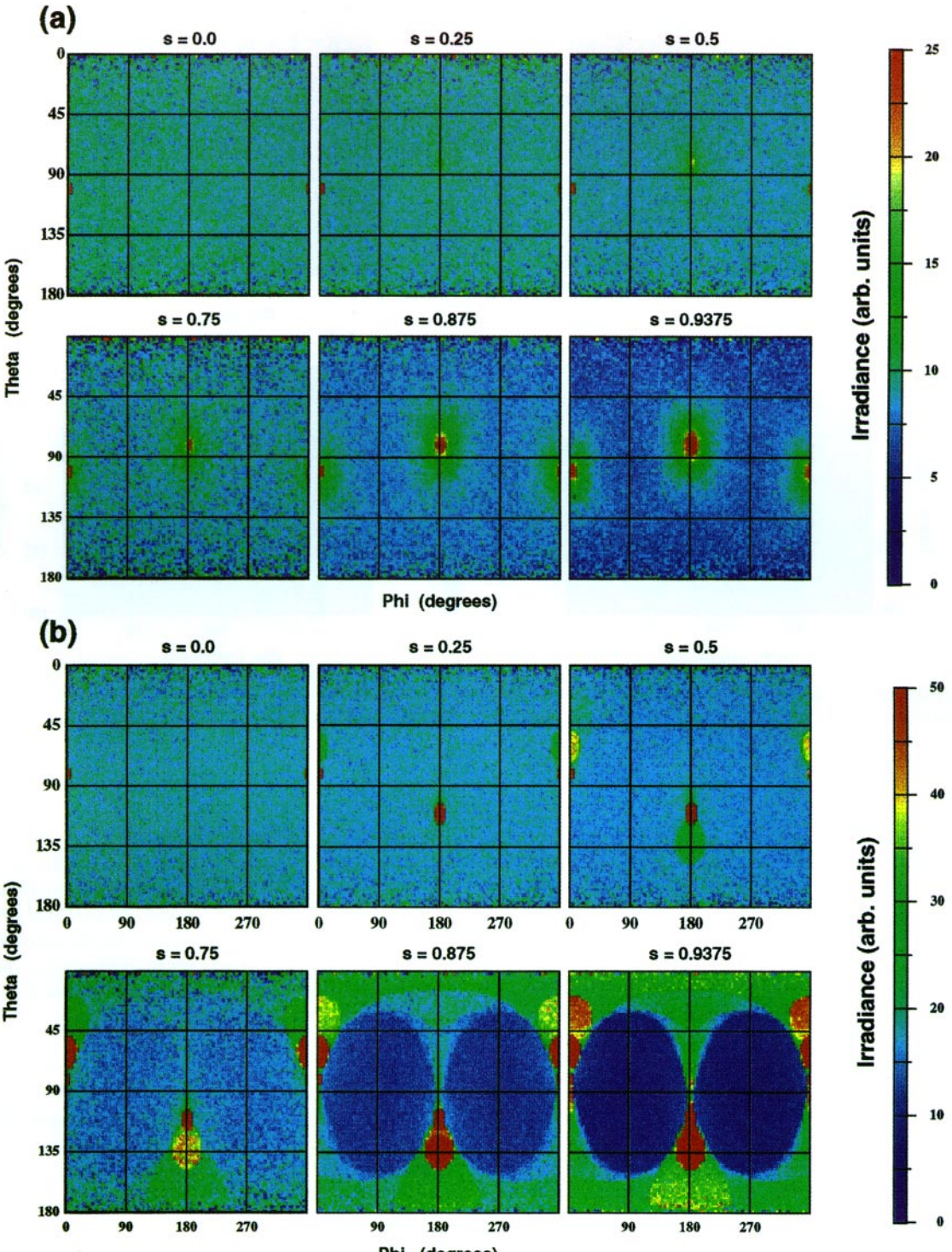
(a)
s = 0.0
s = 0.25
s = 0.5
s = 0.75
s = 0.875
s = 0.9375
Theta (degrees)
Phi (degrees)
Irradiance (arb. units)
(b)
s = 0.0
s = 0.25
s = 0.5
s = 0.75
s = 0.875
s = 0.9375
Theta (degrees)
Phi (degrees)
Irradiance (arb. units)

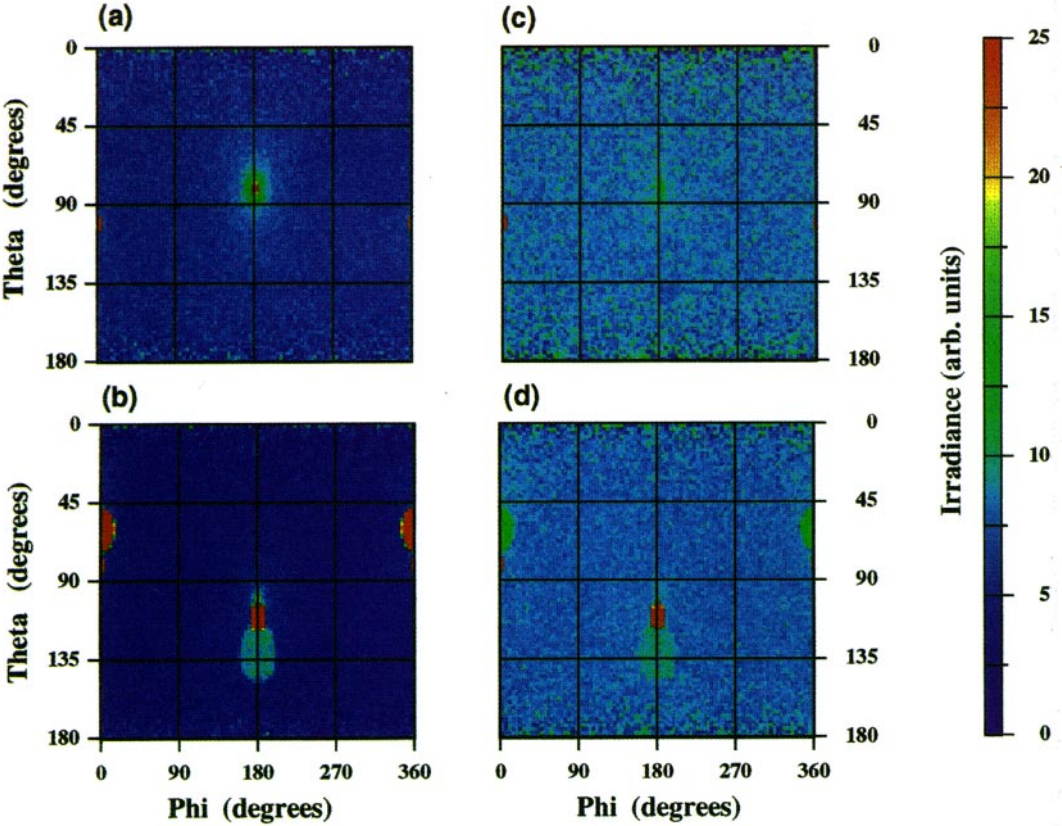
(a)
(b)
(c)
(d)
Theta (degrees)
0
45
90
135
180
Phi (degrees)
0
90
180
270
360
Irradiance (arb. units)
25
20
15
10
5
0